

The numerical comparison of flow patterns and propulsive performances for the hydromedusae *Sarsia tubulosa* and *Aequorea victoria*

Mehmet Sahin^{1,*}, Kamran Mohseni¹ and Sean P. Colin²

¹Department of Aerospace Engineering Sciences, University of Colorado, Boulder, CO 80309, USA and

²Environmental Science/Marine Biology, Roger Williams University, Bristol, RI 02918, USA

*Author for correspondence (e-mail: msahin.ae00@gtalumni.org)

Accepted 29 May 2009

SUMMARY

The thrust-generating mechanism of a prolate hydromedusa *Sarsia tubulosa* and an oblate hydromedusa *Aequorea victoria* was investigated by solving the incompressible Navier–Stokes equations in the swirl-free cylindrical coordinates. The calculations clearly show the vortex dynamics related to the thrust-generating mechanism, which is very important for understanding the underlying propulsion mechanism. The calculations for the prolate jetting hydromedusa *S. tubulosa* indicate the formation of a single starting vortex ring for each pulse cycle with a relatively high vortex formation number. However, the calculations for the oblate jet-paddling hydromedusa *A. victoria* indicate shedding of the opposite-signed vortex rings very close to each other and the formation of large induced velocities along the line of interaction as the vortices move away from the hydromedusa in the wake. In addition to this jet propulsion mechanism, the hydromedusa's bell margin acts like a paddle and the highly flexible bell margin deforms in such a way that the low pressure leeward side of the bell margin has a projected area in the direction of motion. This thrust is particularly important during refilling of the subumbrella cavity where the stopping vortex causes significant pressure drag. The swimming performances based on our numerical simulations, such as swimming velocity, thrust, power requirement and efficiency, were computed and support the idea that jet propulsion is very effective for rapid body movement but is energetically costly and less efficient compared with the jet-paddling propulsion mechanism.

Key words: locomotion, medusae, fluid mechanics, flow patterns, propulsion, computational fluid dynamics, ALE methods, unstructured finite volume.

INTRODUCTION

Over the past two decades, there has been a growing interest in the understanding and prediction of the thrust-generating mechanism of swimming and flying animals. Fluid dynamic phenomena related to swimming and flying animals are generally characterized by relatively low Reynolds numbers (e.g. $Re=1-1000$), complex, variable geometry of the object, large-scale vortex structure because of highly unsteady motions and the interaction of elastic tissue with the surrounding viscous fluid. Extensive reviews in the area of undulatory swimming and flapping flight are given by Lighthill (Lighthill, 1969), Dickinson and colleagues (Dickinson et al., 2000) and Liu (Liu, 2005). These fluid dynamics phenomena are relatively complex because of the interaction between the animal's body motion and the surrounding viscous fluid. However, medusae utilize relatively simple thrust-generating mechanisms and understanding these mechanisms is important for understanding the fundamental principles of animal locomotion.

Medusae propel themselves by contracting a band of circular muscles that line the inner surface of their bell, decreasing the volume of their subumbrellar cavity. This motion ejects water from the oral end of the bell and provides the force to overcome drag which resists motion. The bell kinematics of medusae with prolate-shaped bells (bell height greater than width) creates pulsatile jets and the medusae swim using jet propulsion (Daniel, 1983). The wake of jet-propelled medusae is characterized by a single toroidal rotating ring vortex which is known as the starting vortex ring (Dabiri et al., 2006; Weston et al., 2009). Hydromedusae which swim *via*

jet propulsion are able to adjust the shape of the orifice through which water is ejected from the bell in order to optimize vortex formation, which is thought to minimize the energy cost and maximize the thrust of propulsion (Satterlie, 2002; Dabiri et al., 2006).

Jet propulsion is effective at increasing swimming performance, defined as the ability of a medusa to translate its body throughout the surrounding fluid (Colin and Costello, 2002). Although jet propulsion is effective for rapid body movement, it has been suggested, though not demonstrated, to be energetically costly because the energy expended to accelerate the medusa increases as the square of the medusa's velocity (Ford and Costello, 2000).

These observations indicate that medusae with more oblate bells (i.e. bell height smaller than width) create more complex wake structures than those observed for more prolate jetting medusae, and swim with a jet-paddling mode of propulsion (also termed 'rowing') (Colin and Costello, 2002; McHenry and Jed, 2003). The contraction phase of jet paddling generates a starting vortex similar to that of traditional jetting medusae. However, during the relaxation phase the paddling motion of the bell causes the formation of a second, stopping vortex ring with opposite rotational orientation relative to the starting vortex. These two vortex rings interact and create large induced velocities along the line of interaction as the vortices move away from the hydromedusae in the wake (Dabiri et al., 2005). It has been suggested that the stopping vortex ring has implications not only for swimming but also for hydrodynamic efficiency. Dabiri and colleagues (Dabiri et al., 2007) suggested that the interaction between the starting and stopping vortices acts to

reduce the kinetic energy lost in the wake, thereby increasing the swimming efficiency.

A mathematical model based on the thrust generated by jetting was proposed by Daniel (Daniel, 1983) and the model replicated observed oscillations in swimming speed. Later, Colin and Costello (Colin and Costello, 2002) also found that the mathematical model accurately predicted the body acceleration in prolate medusae, but not oblate medusae. The authors suggested that oblate medusae generate thrust primarily by paddling the flexible margins of their bell instead of using a jet mechanism. However, while the propulsion and fluid interactions of medusae have been well described qualitatively (Colin and Costello, 2002; McHenry and Jed, 2003; Dabiri et al., 2005; Weston et al., 2009), few studies exist that enable the mechanisms of thrust generation in jet paddling to be validated.

We are interested in hydromedusan propulsion as a basis for the design of new propulsion technologies for underwater vehicles. Recently, jet and vortex propulsion have become a focus in the areas of underwater maneuvering and locomotion of bio-engineered vehicles. A vortex thruster loosely mimicking hydromedusa propulsion was proposed by Mohseni (Mohseni, 2004; Mohseni, 2006). The current generation of these thrusters and their implementation on an underwater vehicle are discussed by Krieg and Mohseni (Krieg and Mohseni, 2008) and are capable of producing very strong vortices (formation time of up to 15, see Results for a discussion of formation numbers). Mohseni et al. (Mohseni et al., 2001) and Dabiri and Gharib (Dabiri and Gharib, 2005) also reported numerical and experimental results for jets formed from a nozzle with temporally varying exit velocity and diameter, respectively.

In the present paper, the thrust-generating mechanism of both prolate and oblate medusae is modeled using computational fluid dynamic (CFD) approaches by solving the incompressible

Navier–Stokes equations in the swirl-free axisymmetric cylindrical coordinates in which the azimuthal gradients and velocities are zero. The governing mass and momentum equations are discretized over arbitrary moving Lagrangian–Eulerian control volumes. The continuity equation is satisfied exactly within each element and special attention is given to satisfy the geometric conservation law (GCL) (Thomas and Lombard, 1979) at the discrete level. The equation of motion of a deforming body is solved in addition to the Navier–Stokes equations in a fully coupled form. The mesh deformation is achieved by solving the linear elasticity equation within the fluid domain at each time level while avoiding remeshing in order to enhance numerical robustness. The present numerical method enabled us to demonstrate the vortex dynamics related to the thrust-generating mechanism. In addition, the swimming performances such as swimming velocity, thrust, power requirement and efficiency can be computed directly.

MATERIALS AND METHODS

Computational geometry modeling

To model the flow around swimming hydromedusae we used a geometrically conservative arbitrary Lagrangian–Eulerian (ALE) formulation based upon the bell kinematics of a prolate jetting hydromedusa *Sarsia tubulosa* Sars 1835 and an oblate jet-paddling hydromedusa *Aequorea victoria* Murbach and Shearer 1902. To digitize the bell kinematics during swimming, individual medusae were placed in 64 μm -filtered seawater in glass vessels with dimensions ranging from 4.0 cm \times 8.0 cm \times 1.0 cm to 25.2 cm \times 30.4 cm \times 18.4 cm (width \times height \times depth). The size of the vessel depended upon the size of the medusa; thus we used vessels which allowed an animal to swim freely while still minimizing the depth of field. *Sarsia tubulosa* was video recorded freely swimming using Sony HDR-FX1 (30 frames s^{-1} , 480 \times 640 pixel resolution) and

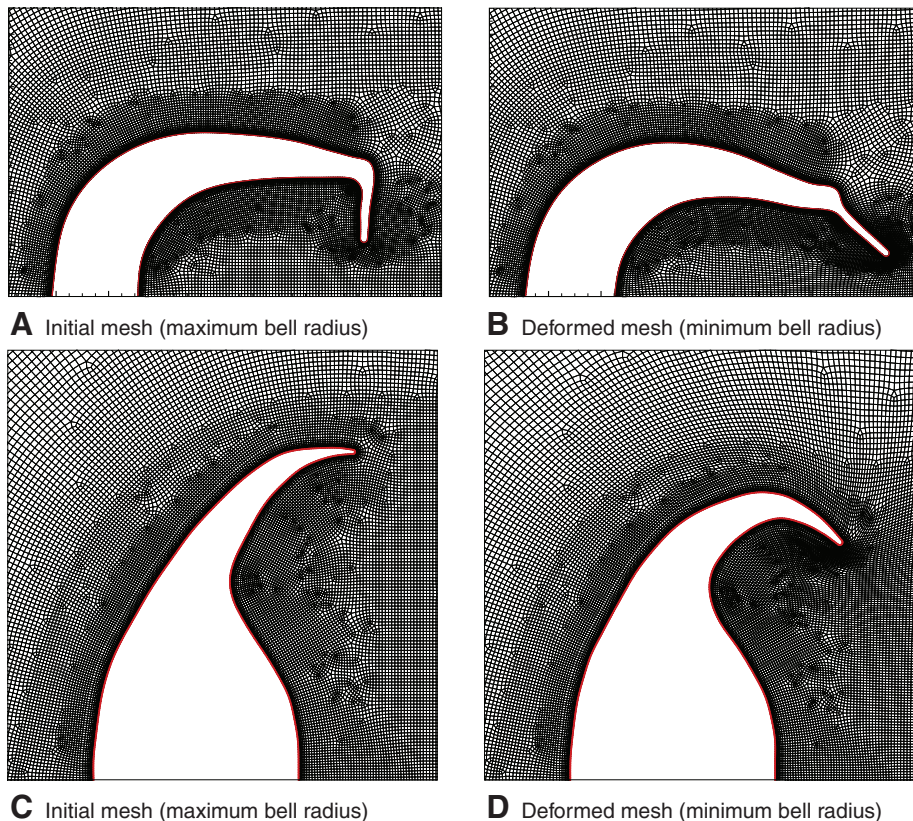


Fig. 1. The computational mesh used for the prolate hydromedusa *Sarsia tubulosa* with 182,517 vertices and 181,730 quadrilateral elements (upper) and the mesh for the oblate hydromedusa *Aequorea victoria* with 205,714 vertices and 204,784 quadrilateral elements (lower).

A. victoria was video recorded using a high definition Basler A504k camera (60 frames⁻¹, 1024×1024 pixel resolution). A laser sheet was directed through the central axis of the medusae to illuminate the outline of the bell. Although the medusae are capable of changing their body density compared with the density of the surrounding water, it was assumed to be equal to the density of water in our numerical simulation. The kinematic viscosity of water was taken to be $\mu/\rho=1\times 10^{-2}\text{cm}^2\text{s}^{-1}$.

To digitize the outline of the medusan bells throughout the pulsation cycle, the geometry of the medusa at each snapshot was approximated by non-uniform rational b-spline (NURBS) curves and Fourier-series interpolation was used in time. The initial computational mesh for the hydromedusa *S. tubulosa* is shown in Fig. 1A. The mesh consists of 182,517 vertices and 181,730 quadrilateral elements. The mesh is highly stretched next to the medusa bell surface in order to resolve the viscous flow within the boundary layer. The rectangular computational domain boundary starts $12D_{\text{max}}$ upstream of the medusa and ends $32D_{\text{max}}$ downstream of the medusa (where D is bell diameter). The lateral far field boundaries are $12D_{\text{max}}$ away from the medusa centroid. The mesh is deformed in every time step by solving the linear elasticity equations within the fluid domain and the mesh corresponding to the minimum bell diameter is shown in Fig. 1B. It is remarkable that even for such a large mesh deformation, the final mesh is totally free from mesh entanglement and remains valid. The initial computational mesh for the hydromedusa *A. victoria* and the maximum deformed mesh are presented in Fig. 1C,D, respectively. The mesh consists of 205,714 vertices and 204,784 quadrilateral elements. The computational domain far field boundary is set to the same parameters as in the hydromedusa *S. tubulosa* mesh.

The governing equations and boundary conditions

The governing equations for the swirl-free axisymmetric Navier–Stokes equations in the cylindrical coordinates system (x, r) can be written over an arbitrary moving Lagrangian–Eulerian control volume $\Omega(t)$ with boundary $\delta\Omega(t)$ in dimensionless form as follows: the continuity equation:

$$-\oint_{\delta\Omega(t)} (ru)dr + \oint_{\delta\Omega(t)} (rv)dx = 0 ; \tag{1}$$

the momentum equations:

$$Re \left[\frac{\partial}{\partial t} \int_{\Omega(t)} (ru)dxdr + \oint_{\delta\Omega(t)} (u-\dot{x})(ru)dr - \oint_{\delta\Omega(t)} (v-\dot{r})(ru)dx \right] + \oint_{\delta\Omega(t)} (rp)dr = \oint_{\delta\Omega(t)} \left(r \frac{\partial u}{\partial x} \right) dr - \oint_{\delta\Omega(t)} \left(r \frac{\partial u}{\partial r} \right) dx , \tag{2}$$

$$Re \left[\frac{\partial}{\partial t} \int_{\Omega(t)} (rv)dxdr + \oint_{\delta\Omega(t)} (u-\dot{x})(rv)dr - \oint_{\delta\Omega(t)} (v-\dot{r})(rv)dx \right] - \oint_{\delta\Omega(t)} (rp)dx - \int_{\Omega(t)} p dxdr = \oint_{\delta\Omega(t)} \left(r \frac{\partial v}{\partial x} + u \right) dr - \oint_{\delta\Omega(t)} \left(r \frac{\partial v}{\partial r} + v \right) dx . \tag{3}$$

In these equations (u, v) are the axial and radial velocity components, respectively; (\dot{x}, \dot{r}) are the axial and radial grid velocity components; p is the pressure; and Re is the dimensionless Reynolds number. For the minus sign in the continuity equation we refer to the review paper by Benzi and colleagues (Benzi et al., 2005). The numerical integration of the above equations over an arbitrary moving

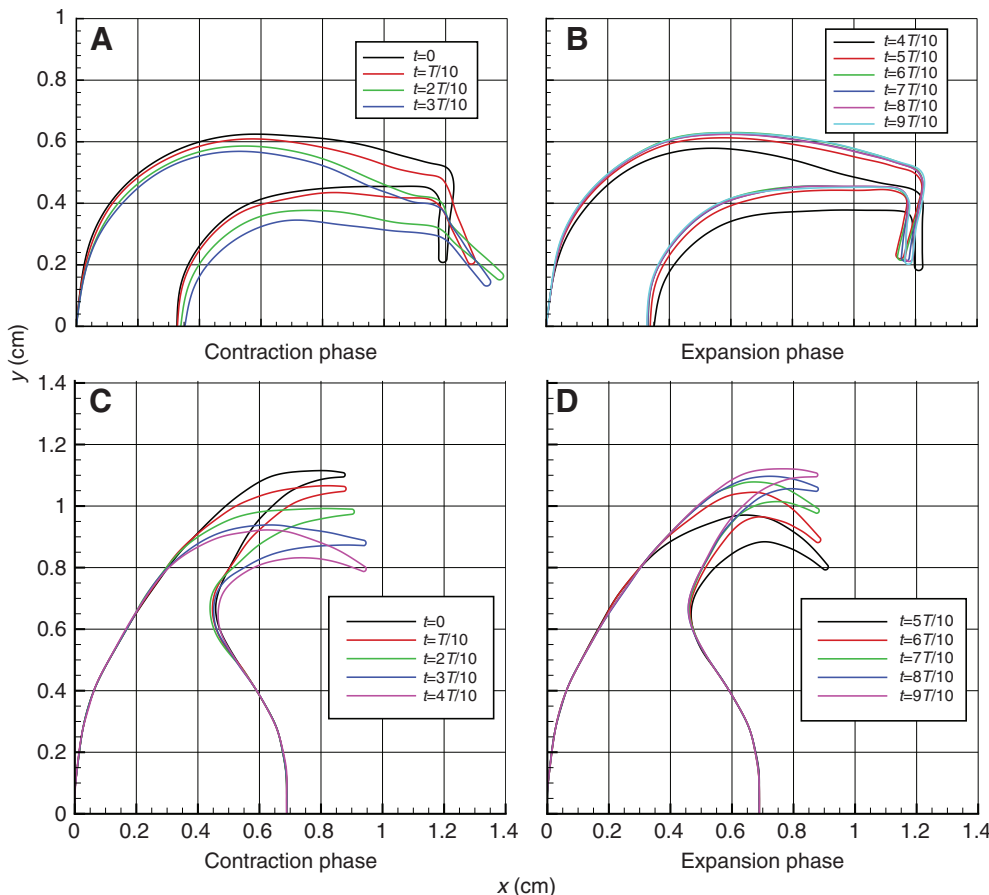


Fig. 2. The time variation of the bell morphology for a free-swimming hydromedusa *S. tubulosa* (upper) and for a free-swimming hydromedusa *A. victoria* (lower). T is the period of one cycle.

Lagrangian–Eulerian control volume should ensure that the GCL (Thomas and Lombard, 1979) is satisfied at the discrete level in order to maintain the accuracy and the stability of the time integration scheme. The GCL equation in the cylindrical coordinate system is given in the following form:

$$\frac{\partial}{\partial t} \int_{\Omega(t)} r dx dr = \oint_{\partial\Omega(t)} r \dot{x} dr - \oint_{\partial\Omega(t)} r \dot{r} dx. \quad (4)$$

This is very similar to the GCL equation in the Cartesian coordinate system.

To compute the velocity of a free-swimming medusa, the following equation of motion is solved in addition to the Navier–Stokes equations in a fully coupled form:

$$V \frac{dU}{dt} = F_x(t), \quad (5)$$

where V is the volume occupied by the medusa, U is the instantaneous velocity of the medusa mass center in a motionless frame and $F_x(t)$ is the total force acting on the medusa in the axial direction, given by:

$$F_x(t) = \frac{2\pi}{Re} \left[-\oint_{\Gamma(t)} (rp) dr + \oint_{\Gamma(t)} \left(r \frac{\partial u}{\partial x} \right) dr - \oint_{\Gamma(t)} \left(r \frac{\partial u}{\partial r} \right) dx \right], \quad (6)$$

where $\Gamma(t)$ defines the time-dependent boundary of the medusa's body. Although the above equations between the medusa velocity U and the Navier–Stokes equations are decoupled they are coupled through the Dirichlet boundary condition on the medusa surface. The far field boundary conditions at the inlet are set to the no-slip zero velocity boundary conditions and the natural (traction-free) boundary conditions at the outlet. Along the axis of symmetry the radial velocity component is set to zero; meanwhile the axial momentum equation is solved numerically for the axial velocity component.

The Froude efficiency (Lighthill, 1975) can be used to evaluate and compare the propulsion efficiency, and it is defined as:

$$\eta = \frac{\langle T \rangle \langle U \rangle}{\langle P \rangle}, \quad (7)$$

where $\langle T \rangle$ is the average thrust due to the pressure term and $\langle P \rangle$ is the average total power supplied by the medusa for one cycle. The

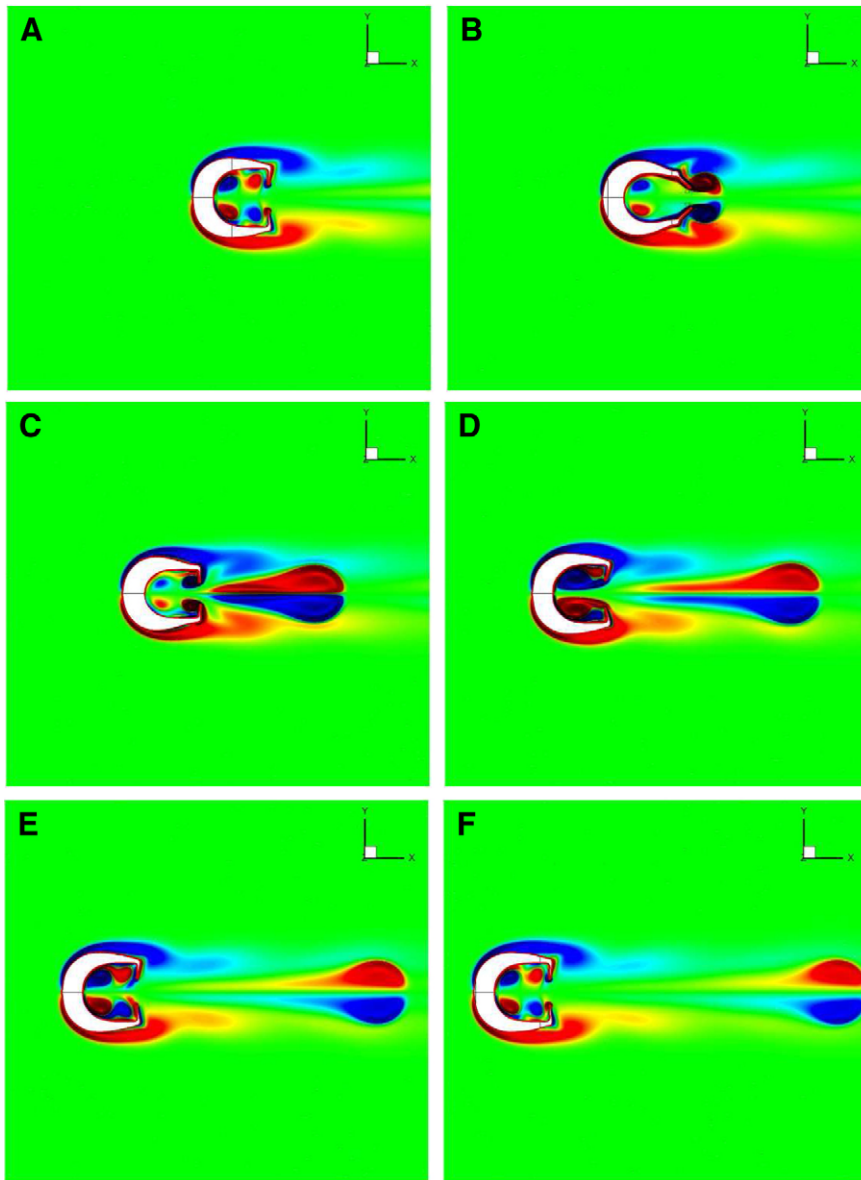


Fig. 3. The sequences of vorticity contours around a free-swimming hydromedusa *S. tubulosa* taken at times $t=t_0$ (A), $t=t_0+T/5$ (B), $t=t_0+2T/5$ (C), $t=t_0+3T/5$ (D), $t=t_0+4T/5$ (E) and $t=t_0+T$ (F), where T is the period of one cycle.

work done by the medusa is computed as a time integral of the power output from its surface to the surrounding fluid:

$$\langle P \rangle = \frac{1}{T} \int_{t_0}^{t_0+T} \oint_{\Gamma(t)} \mathbf{n} \cdot (\boldsymbol{\sigma} \cdot \mathbf{u}) dS dt, \quad (8)$$

where \mathbf{n} is the surface normal vector, $\boldsymbol{\sigma}$ is the stress tensor including the pressure term, S is the surface area defined by $\Gamma(t)$ and \mathbf{u} is the velocity vector on the deforming body surface.

The numerical method

In the present research, a geometrically conservative ALE formulation (an ALE formulation which obeys the GCL) is employed in the swirl-free cylindrical coordinates. In the ALE method, the mesh follows the interface between the fluid and solid boundary and the governing equations are discretized on an unstructured moving and deforming mesh. The governing equations are first multiplied by the radial distance r and then integrated over an arbitrary moving Lagrangian–Eulerian control volume so that the GCL takes a very simple form similar to that of the Cartesian coordinates. In addition, this will allow us to avoid singularities

related to $1/r$ and $1/r^2$ terms in the cylindrical coordinates and will result in better conditioned linear systems. The modified governing equations are discretized by extending the dilation-free semi-staggered finite volume method (Sahin, 2005; Sahin and Wilson, 2007) to the cylindrical swirl-free coordinates, and readers are referred to our previous publication (Sahin and Mohseni, 2009) for the full details of this discretization. The continuity equation is satisfied exactly within each element and special attention is given to satisfy the geometric conservation law at a discrete level. The mesh motion is determined by solving the linear elasticity equation within the fluid domain similar to the work of Dwight (Dwight, 2006) and Johnson and Tezduyar (Johnson and Tezduyar, 1994) at each time level while avoiding remeshing in order to enhance numerical robustness.

RESULTS

Bell kinematics

The digitized bell kinematics of the swimming hydromedusa *S. tubulosa* is shown in Fig. 2A,B. The maximum bell diameter of the medusa was $D_{\max}=1.25$ cm and the period of one cycle T was 1.0 s.

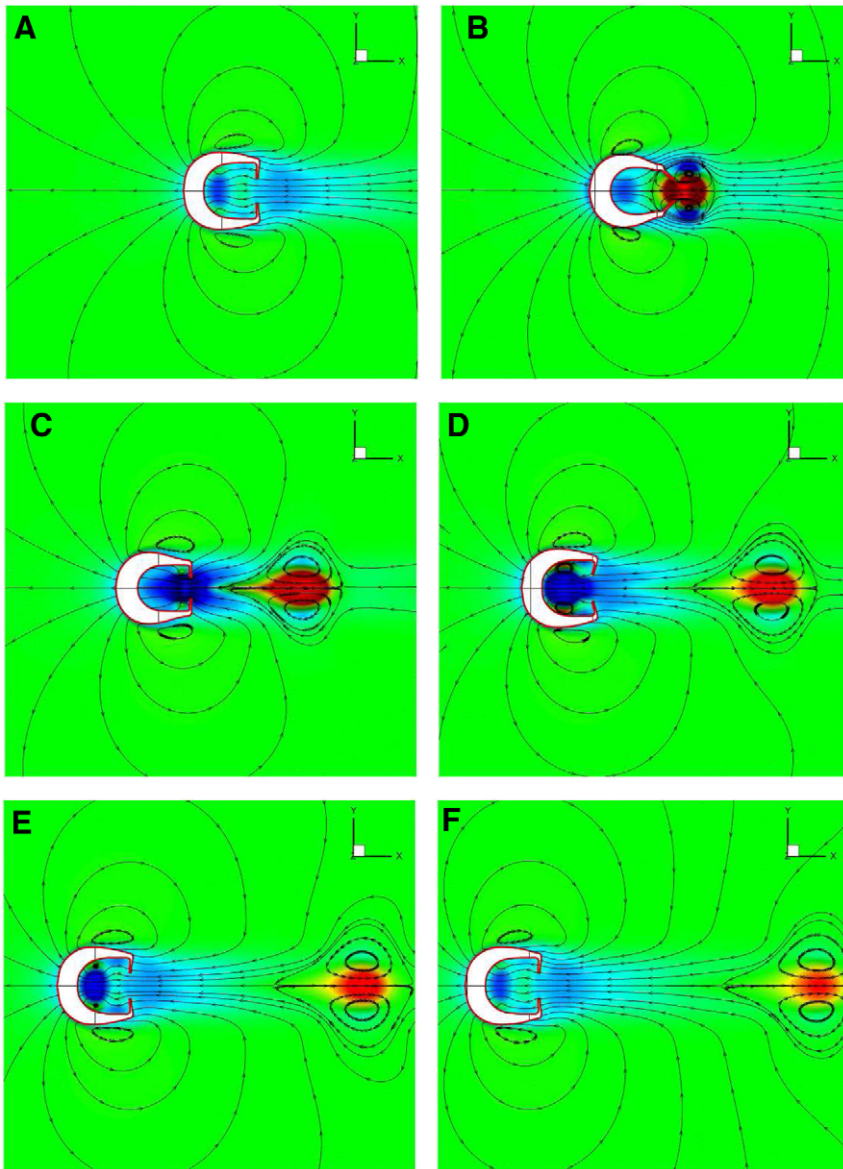


Fig. 4. The sequences of u -velocity component contours with streamlines around a free-swimming hydromedusa *S. tubulosa* taken at times $t=t_0$ (A), $t=t_0+T/5$ (B), $t=t_0+2T/5$ (C), $t=t_0+3T/5$ (D), $t=t_0+4T/5$ (E) and $t=t_0+T$ (F), where T is the period of one cycle.

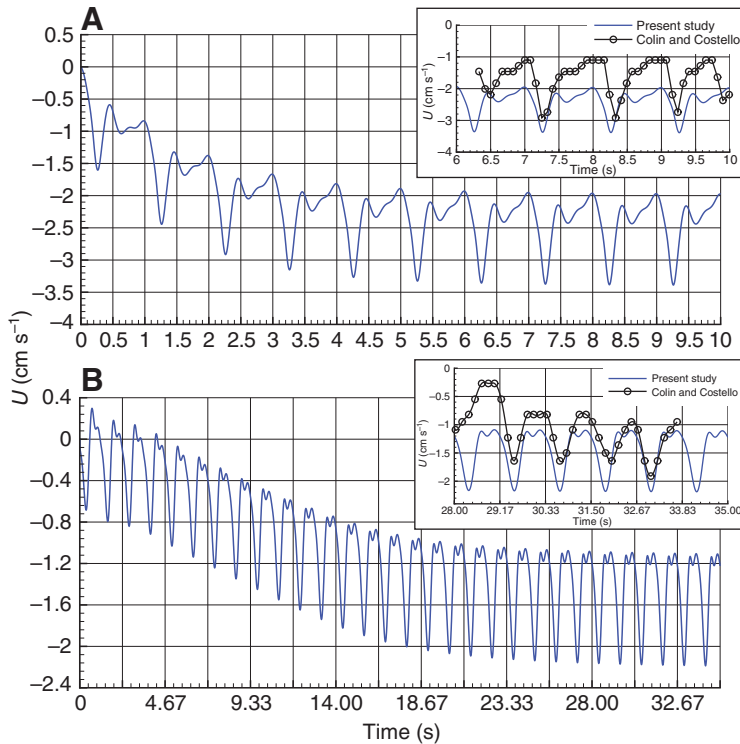


Fig. 5. The instantaneous velocity (U) of free-swimming hydromedusae *S. tubulosa* (A) and *A. victoria* (B) starting from rest, and their comparison with the experimental values of Colin and Costello (Colin and Costello, 1996; Colin and Costello, 2002). The diameters of the hydromedusae *S. tubulosa* and *A. victoria* in the experiments are 0.85 cm and 5.0 cm, respectively.

The maximum contraction ratio of the bell was $D_{\min}/D_{\max}=0.91$. As may be seen from Fig. 2, the bell and velum kinematics were rather complex. In a resting position, the velum was perpendicular to the body axis of radial symmetry. As the bell contracted the pressure inside the subumbrellar cavity caused the velum to take a funnel-shaped form. In addition, the inner diameter of the velum was further reduced. The bell kinematics of the oblate free-swimming

hydromedusa *A. victoria* were obtained by direct video recordings as for the hydromedusa *S. tubulosa* and the time variation of the bell shape is shown in Fig. 2C,D. The maximum bell diameter of the hydromedusa *A. victoria* was $D_{\max}=4.6$ cm and the period of one cycle T was 1.16 s. The maximum contraction ratio of the bell margin was $D_{\min}/D_{\max}=0.72$. Unlike the hydromedusa *S. tubulosa*, the *A. victoria* bell mainly deformed around the bell margin. These

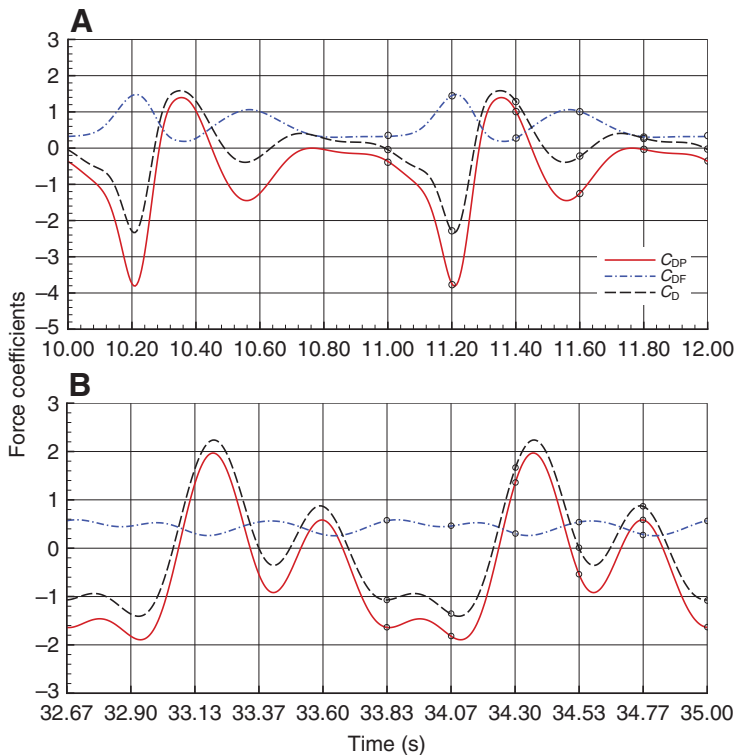


Fig. 6. The time variation of instantaneous force coefficients acting on free-swimming hydromedusae *S. tubulosa* (A) and *A. victoria* (B). C_{DP} is the thrust coefficient, C_{DF} is the skin friction drag coefficient and C_D is the total drag coefficient. The open circles correspond to the times given in Figs 3 and 4 and Figs 7–9. The average thrust coefficients for *S. tubulosa* and *A. victoria* are $\langle C_{DP} \rangle = -0.61$ and $\langle C_{DP} \rangle = -0.43$, respectively.

observations of bell kinematics are consistent with those previously observed for *A. victoria* (Ford and Costello, 2000).

The flow around the hydromedusa *S. tubulosa*

The instantaneous variations of the vorticity field around the free-swimming hydromedusa *S. tubulosa* are presented in Fig. 3 at several time instances. The vorticity field indicates the formation of a single starting vortex ring as the bell contracted during the power stroke. The vortex ring is elongated towards its trailing edge. As the vortex rings move away from the medusa the trailing edge disappears quickly leading to a perfectly circular vortex ring. In addition to the starting vortex, additional vortex rings are formed inside the subumbrellar cavity. However, the increase in the velum diameter and the funnel-shaped velum geometry towards the subumbrellar cavity significantly reduce the vortex ring strength and prevent its interaction with the starting vortex ring during the next contraction. The time evolution of the starting vortex and its location may be seen more clearly from the contours of the u -velocity component with the streamlines given in Fig. 4. From the velocity contours, we did not see any significant trailing flow behind the starting vortex

rings, which is important for the optimal vortex formation (Gharib et al., 1998; Mohseni and Gharib, 1998; Krueger and Gharib, 2003).

Based upon our numerical simulation we calculated the time variation of the instantaneous medusa velocity (Fig. 5A). As is characteristic of the unsteady motion of swimming medusae, there were periodic oscillations in the velocity through time. Based on the average medusa velocity ($\langle U \rangle = 2.42 \text{ cm s}^{-1}$) and the maximum bell diameter, the dimensionless parameters Reynolds $Re = \rho \langle U \rangle D / \mu$ and Strouhal numbers $St = D / \langle U \rangle T$ are computed to be 302 and 0.52, respectively. The total drag coefficient is defined as $C_D = 2F_x / \rho \langle U \rangle^2 \pi (D/2)^2$, and the time variation of the thrust coefficient C_{DP} , the skin friction drag coefficient C_{DF} and the total drag coefficient are also shown against time in Fig. 6A; the open circles represent the time instances corresponding to Figs 3 and 4. As can be seen, the skin friction always acts against the direction of movement. The thrust is mainly created during the ejection of the fluid within the subumbrellar cavity. The second peak around $t = 1.60 \text{ s}$ is due to the refilling process where the high velocity fluid passing through the velum impacts on the subumbrellar cavity surface.

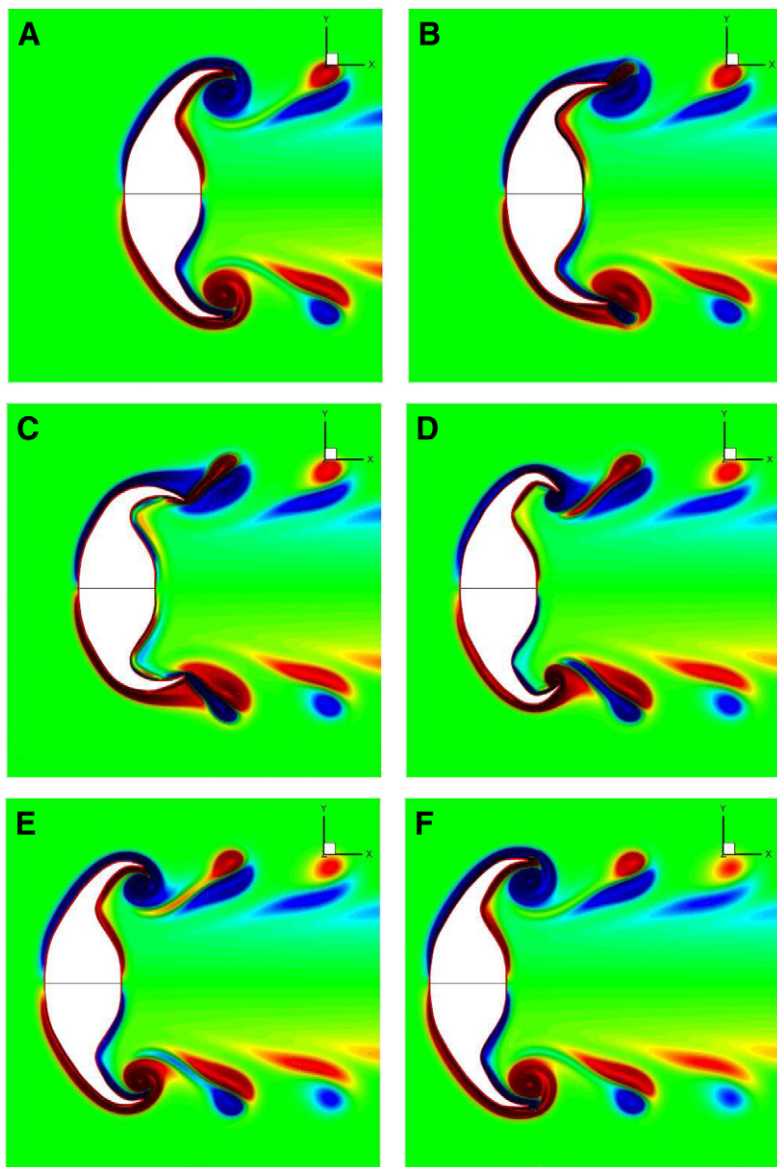


Fig. 7. The sequences of vorticity contours around a free-swimming hydromedusa *A. victoria* taken at times $t = t_0$ (A), $t = t_0 + T/5$ (B), $t = t_0 + 2T/5$ (C), $t = t_0 + 3T/5$ (D), $t = t_0 + 4T/5$ (E) and $t = t_0 + T$ (F), where T is the period of one cycle.

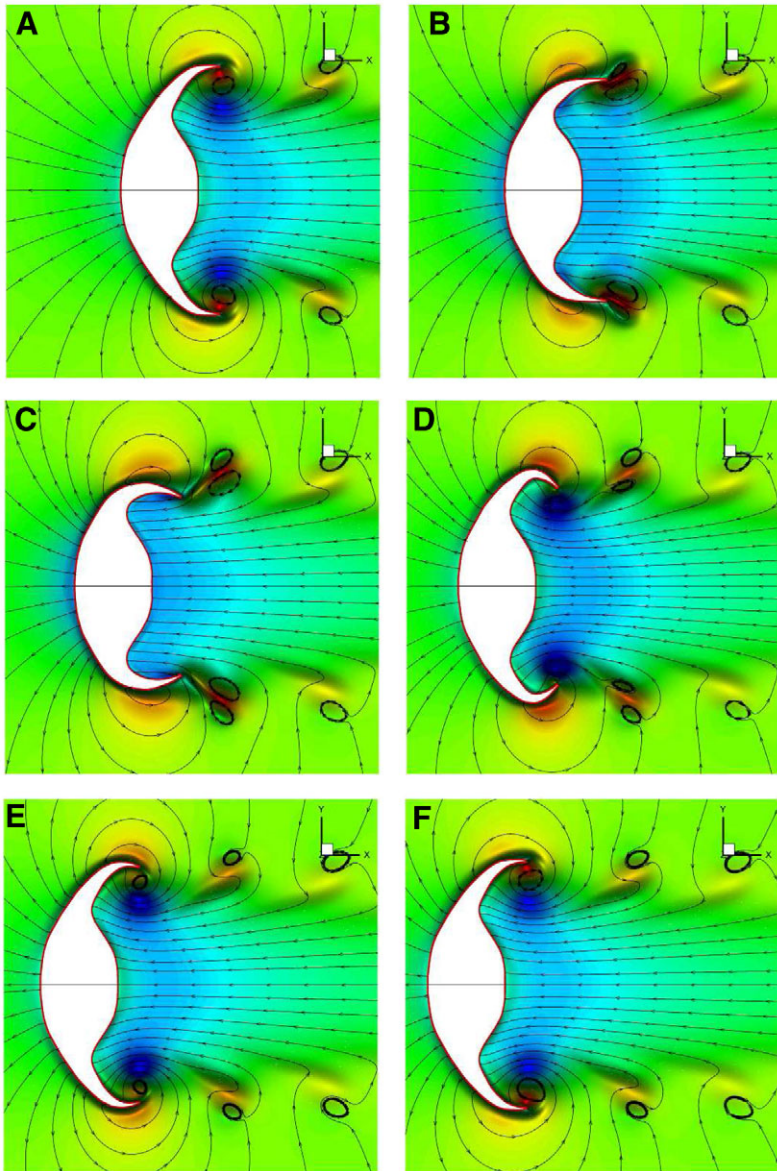


Fig. 8. The sequences of u -velocity component contours with streamlines around a free-swimming hydromedusa *A. victoria* taken at times $t=t_0$ (A), $t=t_0+T/5$ (B), $t=t_0+2T/5$ (C), $t=t_0+3T/5$ (D), $t=t_0+4T/5$ (E) and $t=t_0+T$ (F), where T is the period of one cycle.

The flow around the hydromedusa *A. victoria*

The time variation of the vorticity field around the free-swimming medusa *A. victoria* is given in Fig. 7 at several time instances. The vorticity field indicates the formation of a starting vortex ring as the bell contracted during the power stroke throughout the pulse. The starting vortex ring is formed very close to the opposite-signed stopping vortex ring, which is created within the subumbrellar cavity during the bell relaxation of the previous cycle. Therefore, the starting vortex ring interacts with the stopping vortex within the subumbrellar cavity and creates very large induced velocities along the line of interaction as the vortices move away from the hydromedusae in the wake. The large induced velocities and the location of the vortex rings may be seen more clearly from the contours of the u -velocity component with the streamlines given in Fig. 8. From the streamlines in Fig. 8B,C,D we observe that the induced velocities between the two opposite-signed vortex rings are not exactly parallel to the axis of symmetry even though it is desirable for maximum thrust. Eventually the starting vortex rings form a series of vortex rings in the wake, which generate an opposite force to thrust the medusa body forward. In addition to the jet

propulsion mechanism, the hydromedusa's bell margin acts like a paddle as the hydromedusa rows through the surrounding fluid. This motion creates a low pressure field on the leeward side of the bell margin. If the highly flexible bell margin deforms in such a way that the leeward side of the bell margin has a projected area in the direction of motion, it creates thrust. In fact, this is the case for the pressure contours in Fig. 9D. However, the size of the stopping vortex grows over time, which leads to low pressure within the entire subumbrellar cavity as seen in Fig. 9E. At this point significant pressure drag is caused by the stopping vortex. Surprisingly, this propulsion mechanism creates significant propulsion particularly during refilling of the subumbrellar cavity. Therefore, the oblate hydromedusa *A. victoria* uses both paddling and the jet propulsion mechanism together to propel itself through the surrounding fluid.

The time variation of the instantaneous *A. victoria* medusa velocity is given in Fig. 5B. Similar to *S. tubulosa*, the velocity of *A. victoria* oscillated with each pulsation cycle. Based on the average medusa velocity ($\langle U \rangle = 1.46 \text{ cm s}^{-1}$) and the maximum bell diameter, the dimensionless parameters Reynolds and Strouhal numbers are computed to be 672 and 2.72, respectively. However, if the Strouhal

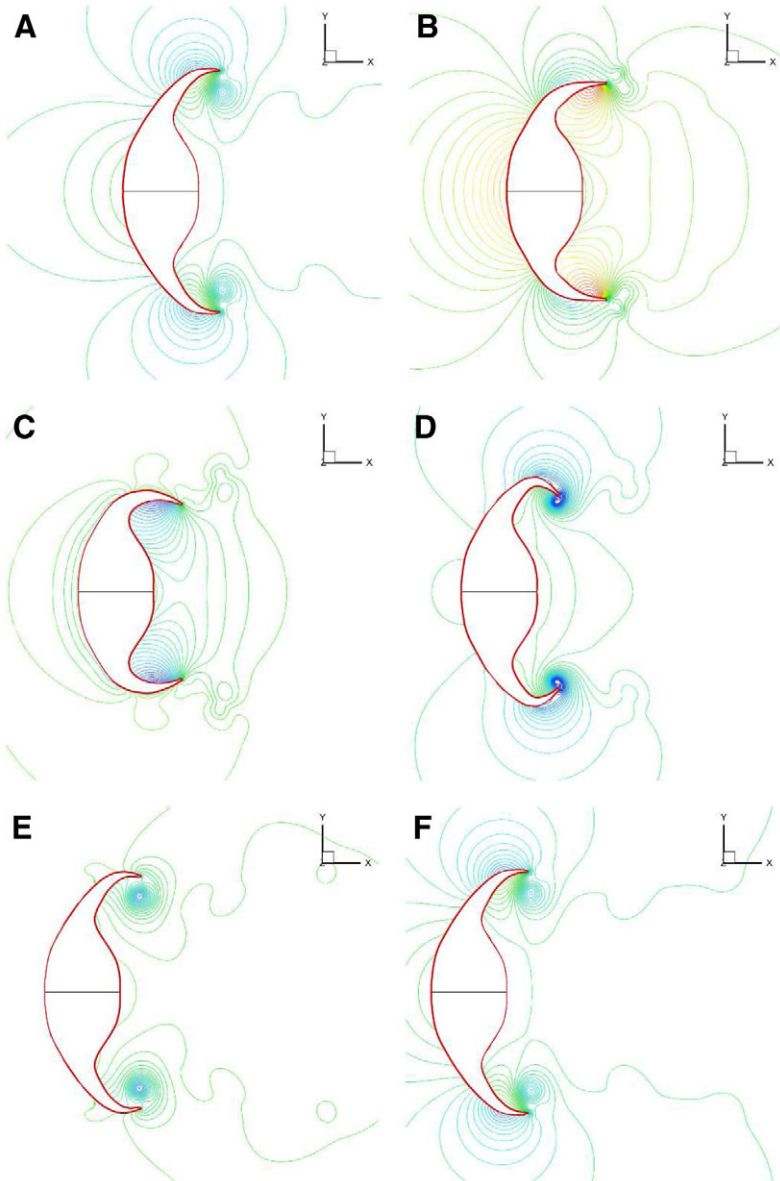


Fig. 9. The sequences of pressure contours for a free-swimming hydromedusa *A. victoria* taken at times $t=t_0$ (A), $t=t_0+T/5$ (B), $t=t_0+2T/5$ (C), $t=t_0+3T/5$ (D), $t=t_0+4T/5$ (E) and $t=t_0+T$ (F). The difference between the contour levels $\Delta p=0.4$. T is the period of one cycle.

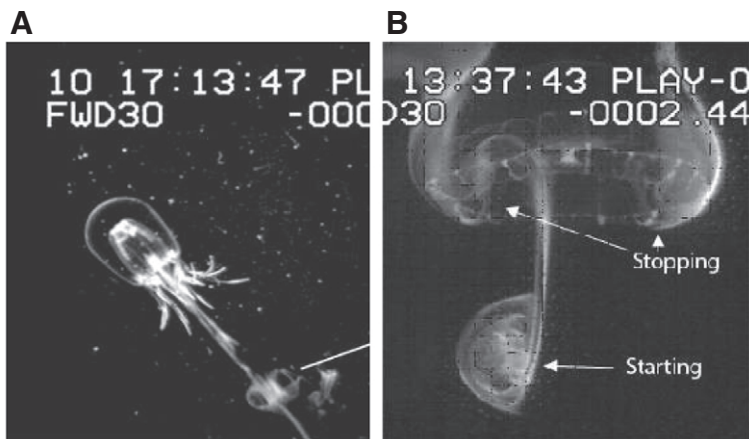


Fig. 10. Dye visualization of the wake structure of (A) *Nemopsis brachei* and (B) *A. victoria* from Dabiri et al. and Weston et al., respectively (Dabiri et al., 2006; Weston et al., 2009).

number is defined analogous to bluff body flows as $St=A/T(U)$, where A is the total excursion of the bell margin, the Strouhal number yields a value of 0.50. The time variation of the thrust coefficient, the skin friction drag coefficient and the total drag coefficient are also shown against time in Fig. 6B and the open circles represent the time instances corresponding to Figs 7, 8 and 9. As can be seen, the skin friction always acts against the direction of movement. Although the thrust coefficient generally acts in the direction of motion, we observe negative effects during the end of the bell contraction phase and just before the end of the bell relaxation phase. The maximum thrust is seen to appear during the formation of the starting vortex ring at $t=34.10$ s. At this point the viscous drag force is also relatively large. The thrust observed during the bell relaxation phase around $t=34.58$ s is due to the paddling motion of the bell margin.

DISCUSSION

Flow visualization and swimming kinematics

The wake structures around swimming prolate and oblate medusae have been well described using dye visualization methods (Dabiri et al., 2005; Dabiri et al., 2006; Colin et al., 2006; Weston et al., 2009). The wake structures observed from our numerical simulations were highly consistent with these previous visualizations using dye. During contraction *S. tubulosa* produced a small starting vortex which did not interact with a stopping vortex and as a result rapidly traveled away from the medusa in the wake. This was very similar to the wake structure of another prolate jetting hydromedusa *Nemopsis brachei* (Fig. 10A). In contrast, flow visualizations from our simulations for the rowing hydromedusa *A. victoria* demonstrated an interaction between the starting and stopping vortices produced during bell contraction and expansion, respectively. Consequently, as has been shown in previous dye visualizations (Fig. 10B) (Dabiri et al., 2005; Colin et al., 2006) and our simulations, a large trailing vortex ring complex can be

observed traveling slowly away from the medusa in the trailing wake. In addition to flow visualizations, the swimming kinematics based on our numerical results are very consistent with the experimental results of Colin and Costello (Colin and Costello, 1996; Colin and Costello, 2002) as shown in Fig 5 for *S. tubulosa* and *A. victoria* with $D_{\max}=0.85$ cm and $D_{\max}=5$ cm, respectively. The numerical results replicate the oscillation seen in the experiments very well. The differences in the velocities observed are likely to be due to differences in size, in that our *S. tubulosa* was about 1.5 times larger than the medusa used by Colin and Costello (Colin and Costello, 2002). These strong similarities in the observed kinematics and flow structures generated by pulsating *S. tubulosa* and *A. victoria* suggest that our simulations accurately model the fluid interactions and energetics of both jetting and jet-paddling medusae.

Characteristics of the wake can be used to estimate the efficiency with which a jet produces thrust. Research on optimal vortex formation has demonstrated that there is an optimal time over which a vortex may be ejected from a jet, and beyond that time the efficiency of the jet declines and a pinched-off secondary vortex is observed in the wake. Experiments using pistons have previously demonstrated that the optimal vortex formation time is $T^*=4$ (Krueger and Gharib, 2003; Gharib et al., 1998). However, mechanisms have been described that can extend this time and delay the pinch off of a secondary vortex (Mohseni and Gharib, 1998; Mohseni et al., 2001; Dabiri and Gharib, 2005). A method of calculating the properties of a slug of fluid from an orifice with variable diameter and velocity was formulated in K.M.'s PhD thesis [see chapter 2 (Mohseni, 2000)]. Using this approach an equivalent vortex formation time (Dabiri and Gharib, 2005) can be defined as:

$$T^* = \int_0^t \frac{U(\tau)}{D(\tau)} d\tau, \quad (9)$$

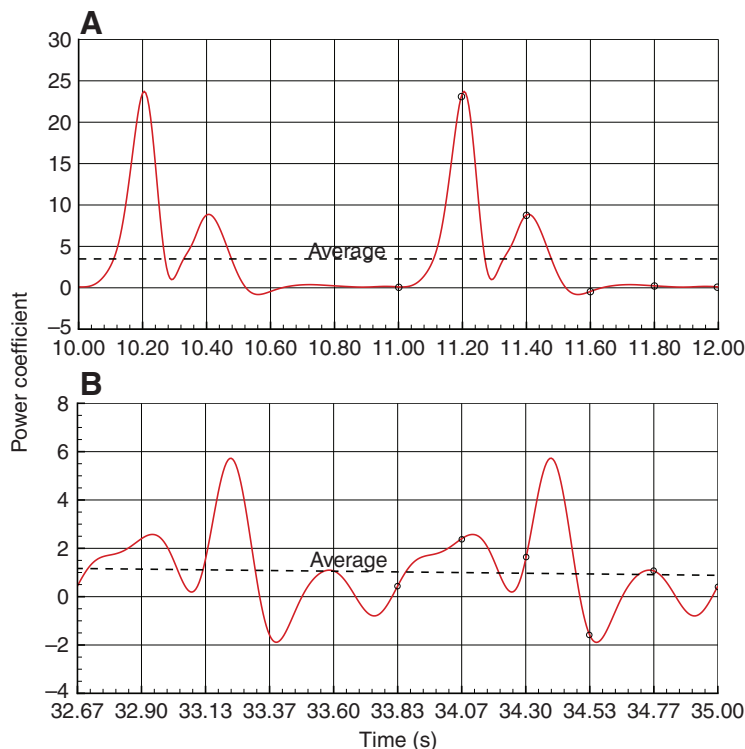


Fig. 11. The time variation of instantaneous power coefficients for free-swimming hydromedusae *S. tubulosa* (A) and *A. victoria* (B). The average power coefficients for *S. tubulosa* and *A. victoria* are $\langle C_p \rangle = 3.55$ and $\langle C_p \rangle = 1.17$, respectively. The open circles correspond to the times given in Figs 3 and 4 and Figs 7–9.

where $t=0$ corresponds to the start of fluid ejection and τ is a dummy variable for the time integral. The vortex formation time for *S. tubulosa* is $T^* \approx 7.4$. This is slightly greater than the vortex formation time ($T^* \approx 4$) that was observed in studies of constant-diameter mechanically generated pulsed jets (Gharib et al., 1998). Consequently, our simulations show *S. tubulosa* delaying the pinch off of the secondary vortex. This can be beneficial because propulsive efficiency declines after the pinch off occurs. Delaying the pinch off enables the medusae to produce more thrust without a loss of efficiency. A similar delay was observed for another jetting hydromedusa *N. bachei*, which was found to have a formation time of $T^* \approx 8$ (Dabiri et al., 2006). Two mechanisms for delaying the pinch off of the leading vortex ring have been suggested (Mohseni and Gharib, 1998). The first is by a time-variable change in the orifice diameter during the vortex formation. The second is by acceleration of the speed of the source flow from the vortex generator in order to prolong the feeding of dynamical invariants (energy, impulse and circulation) to the leading vortex ring. Mohseni and colleagues (Mohseni et al., 2001) reported that significant enhancement of vortex energy, circulation and thrust is achievable using variable-diameter orifices. The velum dynamics described here and by Dabiri and colleagues (Dabiri et al., 2006) change the orifice diameter during contractions and this is thought to be the mechanism by which jetting hydromedusae are able to delay the pinch off of the leading vortex ring (Dabiri et al., 2006). Consequently, in at least some cases velum dynamics in jetting medusae permit the medusae to produce more thrust during bell contraction without substantial loss of efficiency.

The swimming efficiency and the power requirement

The propulsion efficiency of the hydromedusa *A. victoria* is computed to be approximately 37% while the propulsion efficiency of the jetting hydromedusa *S. tubulosa* is 17%. These values confirm the early observations of Ford and Costello (Ford and Costello, 2000) indicating that the oblate medusa had considerably higher efficiencies. Although Ford and Costello computed the swimming efficiency using the Froude efficiency based on the medusa's body velocity and the jet velocity, it considers only the contraction phase and ignores the viscous effects. Dabiri and colleagues (Dabiri et al., 2007) suggested that the interaction between the starting and stopping vortices acts to reduce the kinetic energy lost in the wake, thereby increasing the swimming efficiency for the oblate medusa. However, we believe that the main reason for this is the weaker but larger shed toroidal vortex rings in the wake. Therefore, the total circulation required for the propulsion is achieved and the energy lost is minimized because the energy lost is proportional to $\mu\omega^2$, where μ is the dynamic viscosity and ω is the vorticity. These values are lower than the values reported for most fishes (Sfakiotakis et al., 1999) but higher than the efficiency of microorganisms at very low Reynolds numbers [for example, 2% for the bacterium *Escherichia coli* (Chattopadhyay et al., 2006)]. The low value of the propulsion efficiency is due to the relatively low Reynolds number at which the shed vortex rings dissipate rapidly away from the hydromedusa. The calculations with larger medusa sizes show significant increases in the medusa velocity indicating that the medusae may evolve to much larger sizes and still be able to move through the surrounding fluid. However, the medusa may need to increase the contraction period in order to avoid shear layer instabilities. Otherwise the instabilities may lead to additional energy loss in the wake.

The power coefficient is defined as $C_p = 2P/\rho\langle U \rangle^3 \pi(D/2)^2$ and the time variation of the power coefficients is given for the free-swimming hydromedusae *S. tubulosa* and *A. victoria* in Fig. 11. It is interesting that even though the jetting hydromedusa *S. tubulosa* is very small compared with the hydromedusa *A. victoria*, the average dimensional power requirement is very close to that of the hydromedusa *A. victoria*. For the jetting hydromedusa *S. tubulosa* the power consumption is maximum during the initial stages of the bell contraction. In addition, significant power is needed during refilling of the cavity where the vortex rings created at the velum interact with the subumbrellar cavity surface. For the hydromedusa *A. victoria* the power requirement is maximum during the initial and final stages of the contraction phase. It is noteworthy that the medusa extracts significant power from the fluid during the initial and the final expansion phases of the bell, which is quite different from the case with the jetting medusa.

Conclusions

In conclusion, we were able to use numerical simulations to predict the flow around swimming jellyfish. These simulations quantified the thrust-generating mechanisms and accurately predicted the swimming kinematics and fluid structures generated around jetting and jet-paddling medusae. In addition, despite being several body lengths longer, *A. victoria* swam more efficiently but produced less thrust than *S. tubulosa*, which is consistent with previous predictions about the efficiency versus proficiency of the different propulsive strategies (Colin and Costello, 2002; Dabiri et al., 2005; Dabiri et al., 2006; Weston et al., 2009). Consequently, such simulations may prove to be a useful tool for evaluating the functional morphology of swimming animals.

LIST OF ABBREVIATIONS

<i>A</i>	total excursion of bell margin
ALE	arbitrary Lagrangian–Eulerian
C_D	drag coefficient
C_{DF}	skin friction drag coefficient
C_{DP}	thrust coefficient
C_p	power coefficient
CFD	computational fluid dynamic
D_{max}	maximum bell diameter
D_{min}	minimum bell diameter
F_x	force acting on medusa in axial direction
GCL	geometric conservation law
n	surface normal vector
NURBS	non-uniform rational b-spline
<i>P</i>	power
<i>p</i>	pressure
<i>r</i>	radial distance
\dot{r}	radial grid velocity
<i>Re</i>	Reynolds number
<i>S</i>	surface area
<i>St</i>	Strouhal number
<i>t</i>	time
<i>T</i>	period of one cycle
<i>T</i>	thrust
T^*	vortex formation time
<i>u</i>	axial velocity
<i>U</i>	instantaneous velocity of medusa
u	velocity vector
<i>v</i>	radial velocity
<i>V</i>	volume occupied by the medusa
<i>x</i>	axial distance
\dot{x}	axial grid velocity
Γ	boundary of medusa's body
η	Froude efficiency

μ	dynamic viscosity
ρ	density
σ	stress tensor
τ	dummy variable for time integration
ω	vorticity
Ω	arbitrary moving Lagrangian–Eulerian control volume

K.M., M.S. and S.P.C. would like to acknowledge partial support from the National Science Foundation (OCE-0623534 awarded to S.P.C.) and the Office of Naval Research (ONR N000140810654 subcontract support awarded to S.P.C.) and Air Force Office of Scientific Research for the numerical simulations performed in this investigation. The authors gratefully acknowledge the use of the IBM Machine Bluefire at the National Center for Atmospheric Research.

REFERENCES

- Benzi, M., Golub, G. H. and Liesen, J.** (2005). Numerical solution of saddle point problems. *Acta Numerica* **14**, 1–137.
- Chattopadhyay, S., Moldovan, R., Yeung, C. and Wu, X. L.** (2006). Swimming efficiency of bacterium *Escherichia coli*. *Proc. Natl. Acad. Sci. USA* **103**, 13712–13717.
- Colin, S. P. and Costello, J. H.** (1996). Relationship between morphology and hydrodynamics during swimming by the hydromedusae *Aequorea victoria* and *Aglantha didata*. *Sci. Mar.* **60**, 35–42.
- Colin, S. P. and Costello, J. H.** (2002). Morphology, swimming performance and propulsive mode of six co-occurring hydromedusae. *J. Exp. Biol.* **205**, 427–437.
- Colin, S. P., Costello, J. H. and Kordula, H.** (2006). Upstream foraging by medusae. *Mar. Ecol. Prog. Ser.* **327**, 143–155.
- Dabiri, J. O. and Gharib, M.** (2005). Starting flow through nozzles with temporally variable exit diameter. *J. Fluid Mech.* **538**, 111–136.
- Dabiri, J. O., Colin, S. P., Costello, J. H. and Gharib, M.** (2005). Flow patterns generated by oblate medusan: field measurements and laboratory analysis. *J. Exp. Biol.* **208**, 1257–1265.
- Dabiri, J. O., Colin, S. P. and Costello, J. H.** (2006). Fast-swimming hydromedusae exploit velar kinematics to form an optimal vortex wake. *J. Exp. Biol.* **209**, 2025–2033.
- Dabiri, J. O., Colin, S. P. and Costello, J. H.** (2007). Morphological diversity of medusan lineages constrained by animal–fluid interactions. *J. Exp. Biol.* **210**, 1868–1873.
- Daniel, T. L.** (1983). Mechanics and energetics of medusan jet propulsion. *Can. J. Zool.* **61**, 1406–1420.
- Dickinson, M. D., Farley, C. T., Full, R. J., Koehl, M. A. R., Kram, R. and Lehman, S.** (2000). How animals move: an integrative review. *Science* **288**, 100–106.
- Dwight, R. P.** (2006). Robust mesh deformation using the linear elasticity equations. In *Computational Fluid Dynamics* (ed. H. Deconinck and E. Dick). New York: Springer.
- Ford, M. D. and Costello, J. H.** (2000). Kinematic comparison of bell contraction by four species of hydromedusae. *Sci. Mar.* **64**, 47–53.
- Gharib, M., Rambod, E. and Shariff, K.** (1998). A universal scale for vortex ring formation. *J. Fluid Mech.* **360**, 121–140.
- Johnson, A. and Tezduyar, T.** (1994). Mesh update strategies in parallel finite element computations of flow problems with moving boundaries and interfaces. *Comput. Methods Appl. Mech. Eng.* **119**, 73–94.
- Krieg, M. and Mohseni, K.** (2008). Thrust characterization of a bio-inspired vortex ring generator for locomotion of underwater robots. *IEEE J. Oceanic Eng.* **33**(2), 123–132.
- Krueger, P. S. and Gharib, M.** (2003). The significance of vortex ring formation to the impulse and thrust of a starting jet. *Phys. Fluids* **15**, 1271–1280.
- Lighthill, M. J.** (1969). Hydrodynamics of aquatic animal locomotion. *Annu. Rev. Fluid Mech.* **1**, 413–446.
- Lighthill, M. J.** (1975). *Mathematical Biofluid Dynamics*. Philadelphia, PA: SIAM.
- Liu, H.** (2005). Simulation-based biological fluid dynamics in animal locomotion. *Appl. Mech. Rev.* **59**, 269–282.
- McHenry, M. J. and Jed, J.** (2003). The ontogenetic scaling of hydrodynamics and swimming performance in jellyfish (*Aurelia aurita*). *J. Exp. Biol.* **206**, 4125–4137.
- Mohseni, K.** (2000). Universality in vortex formation. PhD Thesis, California Institute of Technology, Pasadena, CA, USA.
- Mohseni, K.** (2004). Pulsatile jets for unmanned underwater maneuvering. AIAA paper 2004-6386, Chicago, IL, USA. 3rd AIAA Unmanned Unlimited Technical Conference, Workshop and Exhibit.
- Mohseni, K.** (2006). Pulsatile vortex generators for low-speed maneuvering of small underwater vehicles. *Ocean Eng.* **33**, 2209–2223.
- Mohseni, K. and Gharib, M.** (1998). A model for universal time scale of vortex ring formation. *Phys. Fluids* **10**, 2436–2438.
- Mohseni, K., Ran, H. and Colonius, T.** (2001). Numerical experiments on vortex ring formation. *J. Fluid Mech.* **430**, 267–282.
- Sahin, M.** (2005). A preconditioned semi-staggered dilation-free finite volume method for the incompressible Navier–Stokes equations on all-hexahedral elements. *Int. J. Numer. Methods Fluids* **49**, 959–974.
- Sahin, M. and Mohseni, K.** (2009). An arbitrary Lagrangian–Eulerian formulation for the numerical simulation of flow patterns generated by the hydromedusa *Aequorea victoria*. *J. Comput. Phys.* **228**, 4588–4605.
- Sahin, M. and Wilson, H. J.** (2007). A semi-staggered dilation-free finite volume method for the numerical solution of viscoelastic fluid flows on all-hexahedral elements. *J. Non-Newtonian Fluid Mech.* **147**, 79–91.
- Satterlie, R. A.** (2002). Neural control of swimming in jellyfish: a comparative study. *Can. J. Zool.* **80**, 1654–1669.
- Sfakiotakis, M., Lane, D. M. and Davies, J. B. C.** (1999). Review of fish swimming modes for aquatic locomotion. *IEEE J. Oceanic Eng.* **24**, 237–252.
- Thomas, P. D. and Lombard, C. K.** (1979). Geometric conservation law and its application to flow computations on moving grids. *AIAA J.* **17**, 1030–1037.
- Weston, J., Colin, S. P., Costello, J. H. and Abbott, E.** (2009). Changing form and function during development in rowing hydromedusae. *Mar. Ecol. Prog. Ser.* **374**, 127–134.